The extreme blazar AO 0235+164 as seen by extensive ground and space radio observations

A. M. Kutkin,[1][*] I. N. Pashchenko,[1] M. M. Lisakov,[1] P. A. Voytsik,[1]
K. V. Sokolovsky,[1,2,3] Y. Y. Kovalev,[1,4,5] A. P. Lobanov,[5] A. V. Ipatov,[6] M. F. Aller,[7]
H. D. Aller,[7] A. Lahteenmaki,[8,9,10] M. Tornikoski[8] and L. I. Gurvits[11,12]

[1]*Astro Space Center of Lebedev Physical Institute, Profsoyuznaya Str 84/32, 117997 Moscow, Russia*
[2]*Sternberg Astronomical Institute, Moscow State University, Universitetskii pr. 13, 119992 Moscow, Russia*
[3]*IAASARS, National Observatory of Athens, Vas. Pavlou & I. Metaxa, 15236 Penteli, Greece*
[4]*Moscow Institute of Physics and Technology, Dolgoprudny, Institutsky per., 9, Moscow region 141700, Russia*
[5]*Max-Planck-Institut für RadioAstronomie, Auf dem Hügel 69, D-53121 Bonn, Germany*
[6]*Institute of Applied Astronomy of the Russian Academy of Sciences, 191187, Kutuzov embankment, 10, St. Petersburg, Russia*
[7]*Astronomy Department, University of Michigan, Ann Arbor, MI 48109-1042, USA*
[8]*Metsähovi Radio Observatory, Aalto University, Metsähovintie 114, FI-02540 Kylmälä, Finland*
[9]*Department of Electronics and Nanoengineering, Aalto University, PO Box 15500, FI-00076 Aalto, Finland*
[10]*Tartu Observatory, Observatooriumi 1, 61602 Tõravere, Estonia*
[11]*Joint Institute for VLBI ERIC, PO Box 2, NL-7990 AA Dwingeloo, the Netherlands*
[12]*Department of Astrodynamics and Space Missions, Delft University of Technology, Kluyverweg 1, NL-2629 HS Delft, the Netherlands*

ABSTRACT

Clues to the physical conditions in radio cores of blazars come from measurements of brightness temperatures as well as effects produced by intrinsic opacity. We study the properties of the ultra-compact blazar AO 0235+164 with *RadioAstron* ground–space radio interferometer, multifrequency VLBA, EVN, and single-dish radio observations. We employ visibility modelling and image stacking for deriving structure and kinematics of the source, and use Gaussian process regression to find the relative multiband time delays of the flares. The multifrequency core size and time lags support prevailing synchrotron self-absorption. The intrinsic brightness temperature of the core derived from ground-based very long baseline interferometry (VLBI) is close to the equipartition regime value. In the same time, there is evidence for ultra-compact features of the size of less than 10 µas in the source, which might be responsible for the extreme apparent brightness temperatures of up to 10^{14} K as measured by *RadioAstron*. In 2007–2016 the VLBI components in the source at 43 GHz are found predominantly in two directions, suggesting a bend of the outflow from southern to northern direction. The apparent opening angle of the jet seen in the stacked image at 43 GHz is two times wider than that at 15 GHz, indicating a collimation of the flow within the central 1.5 mas. We estimate the Lorentz factor $\Gamma = 14$, the Doppler factor $\delta = 21$, and the viewing angle $\theta = 1.7°$ of the apparent jet base, derive the gradients of magnetic field strength and electron density in the outflow, and the distance between jet apex and the core at each frequency.

Key words: galaxies: active – BL Lacertae objects: individual: 0235+164 – galaxies: jets – radio continuum: galaxies.

1 INTRODUCTION

Blazars are jetted active galactic nuclei (AGN) viewed at a small angle to the line of sight. They appear in very long baseline interferometry (VLBI) images as an unresolved or barely resolved bright core often accompanied by a one-sided jet. Radio emission is produced via the synchrotron mechanism and is boosted by relativistic effects. The core has a flat or inverted spectrum at $cm \, mm^{-1}$ wavelengths and is usually associated with emission from a surface of unit optical depth (Blandford & Königl 1979). The alternative interpretation of the core at mm and sub-mm wavelengths involves shock models (Marscher 2006, 2008). Strong support for the former interpretation comes from the shift between the apparent core

positions measured at different frequencies, first detected by Marcaide & Shapiro (1984). In the framework of this model, the measured core shift can be used to probe jet physics in the core region including the magnetic field strength and its distribution along the outflow, the linear scale of the jet, the jet kinetic energy, etc. (Lobanov 1998; Hirotani 2005). The core shift effect should also be taken into account while contracting and aligning precise celestial reference frames (e.g. Kovalev, Petrov & Plavin 2017; Petrov & Kovalev 2017a,b).

The core shift can be measured directly if a source has a prominent jet, so that one can use its optically thin features as a reference (e.g. Kovalev et al. 2008). There is also an astrometric method to measure the core shift using nearby sources for reference (e.g. Hada et al. 2011). For a compact source the core shift can be estimated indirectly. Opacity is also responsible for changing the angular size of the apparent core measured at different frequencies. Therefore, the dependence of core size on frequency can be linked to the core shift with assumptions about geometry of a jet. Moreover, these measurements allow one to distinguish between intrinsic absorption and scattering in the interstellar medium (e.g. Pushkarev & Kovalev 2015). Finally, the time delays between single-dish light curves at radio bands might also reflect the offset between the core at these frequencies and the outflow velocity (Kudryavtseva et al. 2011; Kutkin et al. 2014).

The radio source AO 0235+164 (hereafter 0235+164; 02:38:38.930107 +16:36:59.27460,[1] J2000) was classified as a BL Lac-type object by Spinrad & Smith (1975) on the basis of its variability and optical spectrum, which appeared featureless at low spectral resolution. Véron-Cetty & Véron (2010) classify the object as QSO based on its absolute magnitude. Cohen et al. (1987) measured the object's redshift detecting Mg II, [Ne V], and [O II] lines at $z = 0.94$. They also found intervening absorption and emission features at lower redshifts. The blazar resides in a field of many faint foreground galaxies (Burbidge et al. 1996; Nilsson et al. 1996) with $z \sim 0.5$, and is often considered to be affected by gravitational lensing (Stickel, Fried & Kuehr 1988; Abraham et al. 1993; Webb et al. 2000).

As seen by VLBI, the source is partially resolved at most radio bands, however its extended structure is very unstable. Gabuzda & Cawthorne (2000) report no detectable milliarcsecond-scale structure, while in other works, some hints of jet-like morphology are reported (see e.g. Jones et al. 1984; Altschuler et al. 1995; Chu et al. 1996, and references therein). Jorstad et al. (2001) detected the jet north-west of the core at 43 GHz and measured the apparent superluminal speed of two components. Later 43 GHz VLBA monitoring revealed the temporary appearance of a component located south-south-east of the core (Agudo et al. 2011, this paper).

The blazar 0235+164 is one of the few brightest sources detected by VSOP and *RadioAstron* space-VLBI missions. Based on VSOP measurements, its brightness temperature is reported to reach $T_b \approx 10^{13.8}$ K (Frey et al. 2000), which challenges the inverse Compton limit even after being corrected for boosting with extremely high Doppler factors.

The source demonstrates violent variability across the electromagnetic spectrum on time-scales from hours to years (e.g. Ackermann et al. 2012 and references in their introduction). The observed cm-wavelength flux density of 0235+164 increases up to 6–7 times during the flaring states. The short-term variability at lower frequencies might be produced by interstellar scintillation (ISS) of newborn ultra-compact VLBI components with a size about 10 μas (Rickett, Lazio & Ghigo 2006). These blobs, in turn, might be responsible for the extremely high brightness temperatures in the source.

In this paper we analyse both VLBI, including Space-VLBI *RadioAstron* data, and single-dish total flux radio observations of 0235+164 to measure multifrequency time lags and core size, derive the brightness temperature and Doppler factor, study the jet structure and estimate its physical and geometrical parameters.

We adopt the standard ΛCDM cosmology model with $H_0 = 71 \, \text{km} \, \text{s}^{-1} \, \text{Mpc}^{-1}$, $\Omega_m = 0.27$, and $\Omega_\Lambda = 0.73$ (Komatsu et al. 2009), which corresponds to a luminosity distance $D_L = 6141$ Mpc, an angular size distance $D_A = 1632$ Mpc, and a linear scale of 7.91 pc mas^{-1} at the source redshift. We use positively defined spectral index $\alpha = \text{d} \ln S / \text{d} \ln \nu$.

2 OBSERVATIONAL DATA

2.1 Ground-based VLBI observations

The blazar 0235+164 was observed on 2008 September 2 with the Very Long Baseline Array[2] (VLBA; Napier 1994), providing baselines of up to 8600 km. The VLBA's frequency agility was used to perform imaging simultaneously at seven frequencies (4.6, 5.0, 8.1, 8.4, 15.4, 23.8, and 43.2 GHz). Eight 8 MHz-wide frequency channels (IFs) were recorded at 128 Mbps with 1-bit sampling. The 5 and 8 GHz data were split into two sub-bands (four IFs each) to provide independent measurements at close frequencies. The observation included 13 on-source scans, each 3–7 min long depending on frequency, spread over 8 h. The data were correlated at the NRAO Array Operation Center in Socorro, NM. This observation was conducted in the framework of our survey of parsec-scale radio spectra of 20 γ-ray bright blazars (Sokolovsky et al. 2010a,b).

Another set of multifrequency observations was performed by the European VLBI Network at 2.3 and 8.4 GHz on 2008 October 19, 5 GHz on 2008 October 22 and 1.7 GHz on 2008 October 29. Each band included eight frequency channels of 8 MHz width each. The 5/1.7 GHz bands were recorded in right and left circular polarizations, while 8.4/2.3 GHz bands where recorded in right circular polarization with a full bitrate of 512 Mbit s^{-1}. The correlation was performed at the Joint Institute for VLBI ERIC (Keimpema et al. 2015).

The a priori amplitude calibration, phase calibration with the phase-cal signal injected during observations, fringe fitting (performed separately for each IF), and bandpass correction were applied in AIPS (Greisen 1990). The hybrid imaging (Walker 1995) including iterations of image deconvolution using the CLEAN algorithm (Högbom 1974) followed by amplitude and phase self-calibration were performed in DIFMAP (Shepherd 1997). We applied a special procedure involving preliminary imaging used to determine residual antenna gain corrections that are persistent in time and appear for all the observed sources (a similar procedure was utilized by Sokolovsky et al. 2011). The resulting amplitude calibration accuracy is expected to be ~5 per cent in the 4.6–15.4 GHz range and ~10 per cent at 23.8 and 43.2 GHz. Details of the calibration and analysis techniques are described by Sokolovsky (2011).

The clean maps of 0235+164 at different frequencies are shown in Fig. 1. Both multifrequency experiments were made during a prominent radio flare in the source.
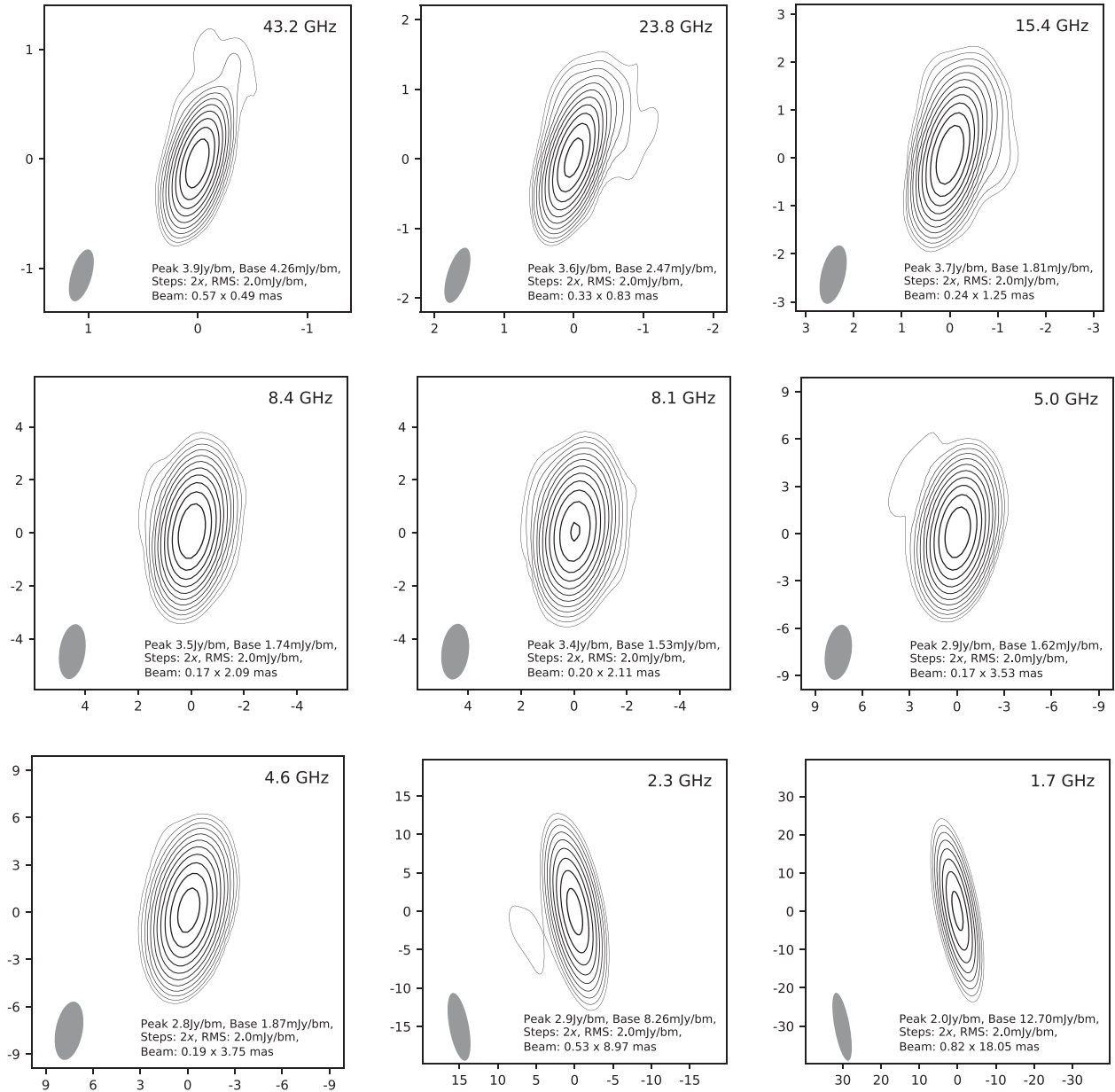
Figure 1. 0235+164 clean maps in RA–Dec. axes. The data at 4.6–43.2 GHz are by VLBA, at 1.7/2.3 GHz – by EVN. The beam size at half-maximum is plotted in the lower left corner.

We have also re-imaged and analysed the calibrated VLBA *uv*-data at 43 GHz by the Boston University blazar group[3] covering 2007–2016 (100 observational epochs). The imaging and model fitting procedures were performed in the same manner as for our multifrequency data.

2.2 Single-dish total flux density observations

The single-dish flux density monitoring observations (Fig. 2) of 0235+164 were obtained with the 26m radio telescope of the University of Michigan Radio Observatory[4] (UMRAO) at 4.8, 8.0, and 14.5 GHz, with the 40m telescope of Owens Valley Radio

Observatory[5] (OVRO) at 15 GHz (Richards et al. 2011), and the 14m telescope of Metsähovi Radio Observatory[6] at 22 and 37 GHz. For the subsequent analysis we merge the complementary 15 GHz data by OVRO and UMRAO.

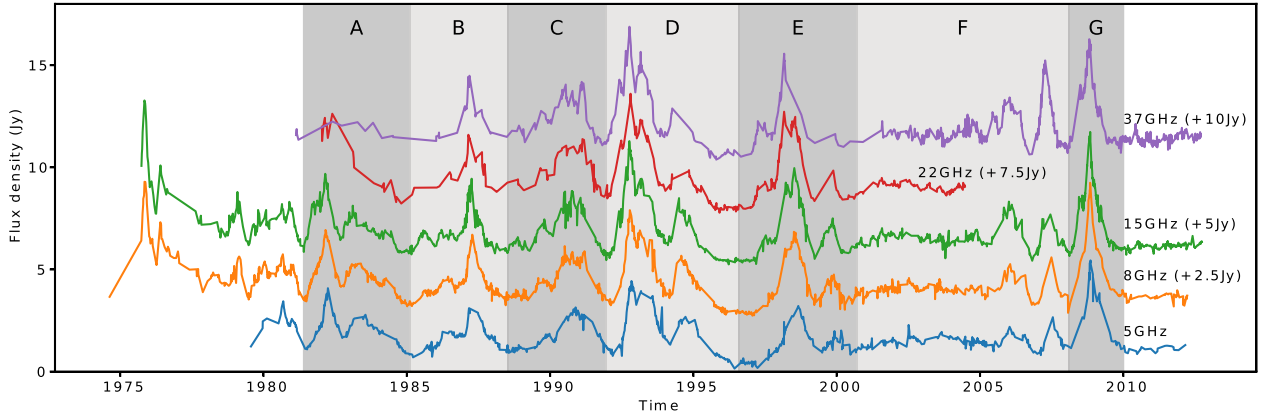### 2.3 *RadioAstron* space-VLBI observations

The blazar 0235+164 is a target of the *RadioAstron* AGN Survey (Kovalev et al. in preparation). It is monitored regularly at 1.6, 4.8, and 22.2 GHz by the space radio telescope antenna along with ground-based telescopes in interferometric mode. A typical observational set covers 40–60 min and is performed either in a

---

Figure 2. The single-dish total flux density light curves of AO 0235+164 at 4.8–37 GHz shifted along *y*-axis for better visualization. Shaded areas denote the epochs of interest, see Section 4 for details.

single band with two circular polarizations or in two bands with one circular polarization of opposite sense per band. Correlation was performed at the Astro Space Center using a software correlator (Kardashev et al. 2013; Likhachev et al. 2017). Post-correlation handling (fringe fitting, calibration) was performed using PIMA[7] software (Petrov et al. 2011). We analysed 12 observational epochs from 2012 December through 2016 January, as summarized in Table 3.

3 VLBI ANALYSIS

We modelled the VLBI structure of 0235+164 at each frequency in the *uv*-plane using DIFMAP. The *K*-fold cross-validation (Hastie, Tibshirani & Friedman 2009) was used to select the best model among a point source, elliptical and circular Gaussian shape of the core (the other components, if any, were modelled with circular Gaussian profiles). This method is aimed to estimate prediction performance of a model on a new data based on the data at hand. It employs the data splitting into *K* non-overlapping sub-samples. Then the following steps are done: one sub-sample is excluded from the data, the model is fitted to the rest *K* − 1 sub-samples, and its prediction performance (score) for the excluded subset is evaluated (e.g. by calculating residuals RMS). This procedure is repeated *K* times with changing the excluded subset. The average score of the obtained *K* values characterizes how the model can generalize (i.e. describes an arbitrary new data), and is used for comparison of different models. We apply this method to the calibrated *uv*-data and the models constructed in DIFMAP. To ensure that all the baselines are represented evenly during the procedure we performed the splitting at each one separately. We also varied *K* in the range 3–10 for the sake of robustness. The elliptical Gaussian model was found to better describe the core. We note, that the extended structure, if any, is weak and does not affect core parameters significantly. The errors in the model parameters were estimated in the image plane following Fomalont (1999).

Additionally, we compared the size of the fitted core with the resolution limit suggested by Kovalev et al. (2005) for a Gaussian brightness distribution template. The core is resolved at all frequencies except for 1.7 GHz and at almost all epochs of the 7 mm long-term monitoring data. If the core was unresolved, we used the corresponding resolution limit for its major and minor axes

Table 1. Source models for the two multifrequency experiments. Columns: (1) frequency, (2) component ID, (3–8) standard Difmap format: flux density, distance, position angle, major axis, axial ratio, major axis orientation angle.

Freq. (GHz) (1)	ID (2)	S (Jy) (3)	R (mas) (4)	θ_c (deg) (5)	b_{maj} (mas) (6)	e (7)	Φ (deg) (8)
43.2	C0	3.498	0.027	171	0.058	0.56	7.7
	C1	0.636	0.146	−178	0.064		
	C2	0.051	0.149	113	<0.001		
	C3	0.062	0.613	−18	0.837		
23.8	C0	3.714	0.015	2	0.115	0.43	24.0
	C1	0.046	0.204	88	0.174		
	C2	0.110	0.634	−22	0.714		
15.37	C0	3.714	0.059	−2	0.125	0.50	28.0
	C1	0.163	0.725	−18	0.821		
8.43	C0	3.378	0.038	−28	0.197	0.56	−13.6
	C1	0.258	0.686	−23	0.802		
8.11	C0	3.288	0.035	−51	0.196	0.45	−26.3
	C1	0.247	0.729	−23	0.772		
5.0	C0	2.758	0.057	−42	0.328	0.57	−10.9
	C1	0.288	0.669	−22	1.127		
4.61	C0	2.642	0.097	−39	0.346	0.51	−16.8
	C1	0.297	0.678	−22	1.189		
8.39	C0	6.457	0.049	−173	0.197	0.56	5.0
	C1	0.374	0.447	−21	0.655		
	C2	0.015	1.550	79	1.001		
4.97	C0	4.897	0.032	143	0.290	0.46	0.7
	C1	0.414	0.588	−16	1.003		
2.27	C0	2.987	0.057	−163	0.772	0.73	−11.0
	C1	0.015	2.864	−48	<0.001		
	C2	0.037	6.164	112	5.684		
1.66	C0	2.069	0.093	19	<1.590	0.60	2.1
	C1	0.010	4.315	61	<0.001		
	C2	0.010	4.902	−24	0.009		

size. Models for the multifrequency experiments are summarized in Table 1.

4 LIGHT CURVES ANALYSIS

The variability time delays between light curves can be found using several methods based either on data modelling or cross-correlation techniques. The former implies some prior knowledge about the data (e.g. Gaussian shapes of the flares, Pyatunina et al. 2007;

---

[7] http://astrogeo.org/pima

Kudryavtseva et al. 2011) or two-sided exponential profiles (Valtaoja et al. 1999; Hovatta et al. 2009). Moreover, one has to manually distinguish separate flares profiles, which is the subject of errors due to the Human factor. The latter methods are based on calculation of mutual cross-correlation function (CCF) of the light curves and do not involve additional information about their structure (e.g. standard correlation function with interpolation (ICCF) or discrete correlation function (DCF; Edelson & Krolik 1988). However, these methods require a sufficient amount of data to perform well and also require some parameters choice that may affect the results, like the bin width used for interpolation and DCF evaluation (see White & Peterson 1994 for ICCF/DCF comparison and references).

Another approach, which also does not require any prior knowledge about the data is based on the Gaussian process regression (GPR; Rasmussen & Williams 2005) – a special case of Bayesian non-parametric models. It has been recently applied to the light curves of the blazar PKS 1502+106 by Karamanavis et al. (2016).

Gaussian process (GP) is a probability distribution over functions. It is characterized by its mean value and covariance matrix. The former can be set to zero by shifting the data, the latter is expressed through the covariance function (*kernel*). The kernel depends on *hyperparameters*, which are inferred for a given data set by maximizing the marginal likelihood function (*training* the GP).

Any GP realization can be considered as a function (in case of time series this is the function of time). The often-used GP kernel for time series is the 'squared exponential' (SE):

$$C_{SE}(t_i, t_j) = A^2 \exp\left(\frac{-(t_i - t_j)^2}{2l^2}\right), \tag{1}$$

where C is the covariance between the function values at arbitrary times t_i and t_j, l and A are the hyperparameters that correspond to the characteristic time-scale and amplitude of function variations.

In the case of longer light curves containing several or multi-peaked flares the single SE kernel (1) might not perform well due to the presence of more than one characteristic scale in the source variability. This is the case for blazars, which are known to vary on a range of time-scales and usually possess 'red' power spectra (e.g. Max-Moerbeck et al. 2014, and references therein). To overcome this problem one may use a sum of several SE-kernels. Such a weighted sum is represented by the rational quadratic (RQ) kernel (Rasmussen & Williams 2005, Chapter 4):

$$C_{RQ}(t_i, t_j) = A^2 \left(1 + \frac{(t_i - t_j)^2}{(2\varepsilon l^2)}\right)^{-\varepsilon}. \tag{2}$$

The relative weighting of different time-scales variations is specified by the hyperparameter $\varepsilon \in (0, +\infty)$. In the limit of $\varepsilon \to +\infty$ the RQ kernel becomes an SE kernel.

We use a kernel represented by a sum of the RQ-kernel and the White kernel characterizing the noise:

$$C(t_i, t_j) = C_{RQ}(t_i, t_j) + \delta_{ij}\left(\sigma_{obs}^2 + \sigma_n^2\right), \tag{3}$$

with the hyperparameters A, l, ε of the RQ-kernel. σ_{obs} are the measurements uncertainties of the data, and the additional σ_n is used to describe the possible unaccounted noise (*jitter*). δ_{ij} is the Kronecker delta.

The hyperparameters are inferred by maximizing the following marginal likelihood function:

$$\mathcal{L} = \log p(\boldsymbol{y}|\boldsymbol{t}, \boldsymbol{\Theta}) = -\frac{1}{2}\boldsymbol{y}^T C^{-1}\boldsymbol{y} - \frac{1}{2}\log|C| - \frac{n}{2}\log 2\pi, \tag{4}$$

where $\boldsymbol{\Theta}$ is the vector of the hyperparameters, and $p(\boldsymbol{y}|\boldsymbol{t}, \boldsymbol{\Theta})$ is the probability of realization of the observed flux density values

$\boldsymbol{y} = \{y_1, \ldots, y_n\}$ at the times $\boldsymbol{t} = \{t_1, \ldots, t_n\}$ for the given $\boldsymbol{\Theta} = \{A, l, \epsilon, \sigma_n\}$. Then, using the obtained hyperparameters and the data at hand one can obtain the mean value of the GP realizations and its corresponding confidence interval at any time point t_k, i.e. obtain the regression model for the light curve with the uncertainties (Rasmussen & Williams 2005).

The GPR constructed as described above, however, does not account for the uncertainties of the estimated hyperparameters. This can be incorporated by sampling the posterior distributions of the hyperparameters with Markov chain Monte Carlo (MCMC) method. For that purpose we employed EMCEE sampler (Foreman-Mackey et al. 2013) and GEORGE PYTHON library (Ambikasaran et al. 2015). We used uniform priors for the hyperparameters. From the obtained samples of the joint posterior distributions we drew a number of the hyperparameters vectors $\boldsymbol{\Theta}$ and constructed the realizations of the GP. For each realization we measured time and flux density of the flares peaks and used their scatter for the uncertainties estimation.

To check whether there is a difference between time lags at different epochs we split our data manually into seven time intervals each having at least one prominent outburst. This was done to perform cross-correlation analysis (see below). The selected intervals are denoted in Fig. 2. The results are summarized in Table 2. As an example, the results of implementing GPR to the 15 GHz light curve of epochs interval 1985–1988 (labelled B) are shown in Fig. 3. The histograms illustrate the resulting posterior distributions of the hyperparameters (the plot is produced with CORNER package by Foreman-Mackey 2016). Median and 16/84 percentiles are shown by vertical lines. In the upper right corner the light curve is shown along with $\pm 3\sigma$ (99.7 per cent) confidence interval for GPR. Note the outlying data point near the flare peak. Its sharpness and absence of the counterparts at other frequencies suggest its 'extrinsic' nature presumably due to measurements error. The outlier is effectively bypassed by the GPR method, which indicates the low probability of it to belong to the model. The hyperparameter σ_n shows the level of an additional unaccounted noise in data at the level about 0.1–0.2 Jy, which is comparable with the data uncertainties. Thus, using the jitter in our kernel provides more realistic uncertainties of the T_m and F_m. As expected, the confidence interval widens within data gaps. The separate flares and the corresponding time delays are shown in Fig. 5.

We also apply the DCF method to the time intervals labelled in Fig. 2. To estimate the errors of the resulting delays we perform Monte Carlo simulations and modified bootstrapping [or flux randomization/random sub-sample selection (FR/RSS) method proposed by Peterson et al. 1998]. This allows us to account for errors due to initial flux-measurement uncertainties as well as for the data outliers. To account for the possible influence of the time bin selection we varied it in each simulation to be uniformly spread in the range $[0.5, 1.5]\Delta t_{mean}$ (where Δt_{mean} is the mean time span between the observations). Example of the DCF results for the G-flare at 37–15 GHz is shown in Fig. 4 along with the obtained distribution of the time lags. In general, the DCF results are similar to that by GPR but the wide resulting distributions of the time delays give higher uncertainties. Moreover, the DCF results are affected by the selection of a light-curve length. The following discussion is based on the results obtained with the GPR method.

5 VARIABILITY TIME DELAYS

We approximated the dependence of the time lags ΔT on frequency ν (comparative to the peak at highest one) with the model $\Delta T = a_t(\nu/GHz)^{-k_t} + b_t$. To find the parameters we used the

Table 2. GPR results: the peak time (T_m, MJD) and flux density (F_m, Jy) of the flares at 4.8–37 GHz. The values are median, 84/16 percentiles (and median absolute deviation in brackets).

		37 GHz	22 GHz	15 GHz	8 GHz	4.8 GHz
A1	T_m	–	–	$45\,030^{+2}_{-1}(1.4)$	$45\,034^{+2}_{-2}(1.8)$	$45\,057^{+6}_{-5}(5.9)$
	F_m	–	–	$4.53^{+0.04}_{-0.04}$	$4.30^{+0.02}_{-0.03}$	$3.65^{+0.07}_{-0.06}$
B1	T_m	$46\,866^{+14}_{-9}(10.3)$	$46\,857^{+5}_{-17}(8.8)$	$46\,888^{+8}_{-3}(5.5)$	$46\,900^{+3}_{-3}(2.9)$	$46\,913^{+15}_{-8}(11.9)$
	F_m	$4.49^{+0.22}_{-0.14}$	$4.15^{+0.21}_{-0.13}$	$4.09^{+0.03}_{-0.04}$	$4.01^{+0.05}_{-0.05}$	$3.32^{+0.19}_{-0.21}$
D1	T_m	$48\,904^{+4}_{-3}(3.4)$	$48\,912^{+5}_{-4}(5.1)$	$48\,903^{+1}_{-1}(0.9)$	$48\,911^{+1}_{-1}(1.1)$	$48\,930^{+1}_{-4}(2.2)$
	F_m	$6.70^{+0.13}_{-0.11}$	$5.84^{+0.10}_{-0.09}$	$6.11^{+0.04}_{-0.05}$	$5.31^{+0.04}_{-0.04}$	$4.17^{+0.02}_{-0.02}$
E1	T_m	$50\,873^{+3}_{-3}(2.8)$	$50\,876^{+3}_{-2}(2.4)$	$50\,907^{+10}_{-8}(9.1)$	–	–
	F_m	$5.30^{+0.13}_{-0.10}$	$5.08^{+0.07}_{-0.07}$	$4.01^{+0.07}_{-0.07}$	–	–
E2	T_m	–	$51\,001^{+5}_{-8}(6.6)$	$51\,015^{+4}_{-3}(3.8)$	$51\,008^{+2}_{-2}(2.1)$	$51\,027^{+7}_{-10}(8.0)$
	F_m	–	$4.80^{+0.14}_{-0.14}$	$4.56^{+0.15}_{-0.15}$	$4.18^{+0.04}_{-0.05}$	$3.25^{+0.03}_{-0.05}$
E3	T_m	–	–	$51\,492^{+1}_{-2}(1.6)$	$51\,496^{+7}_{-5}(6.2)$	$51\,530^{+3}_{-4}(3.7)$
	F_m	–	–	$2.30^{+0.02}_{-0.02}$	$2.02^{+0.05}_{-0.04}$	$1.66^{+0.02}_{-0.01}$
F1	T_m	$53\,723^{+9}_{-13}(11.7)$	–	$53\,752^{+7}_{-6}(6.3)$	$53\,763^{+5}_{-4}(4.6)$	$53\,752^{+1}_{-2}(1.5)$
	F_m	$3.42^{+0.12}_{-0.13}$	–	$3.26^{+0.04}_{-0.04}$	$2.62^{+0.04}_{-0.04}$	$2.06^{+0.02}_{-0.01}$
F2	T_m	$54\,203^{+4}_{-4}(3.7)$	–	$54\,251^{+14}_{-12}(13.1)$	$54\,269^{+6}_{-8}(7.3)$	$54\,290^{+7}_{-6}(6.8)$
	F_m	$4.96^{+0.11}_{-0.11}$	–	$2.78^{+0.14}_{-0.09}$	$3.09^{+0.08}_{-0.07}$	$2.39^{+0.09}_{-0.09}$
G1	T_m	$54\,764^{+3}_{-2}(2.7)$	–	$54\,770^{+1}_{-0}(1)$	$54\,774^{+1}_{-2}(1.2)$	$54\,784^{+2}_{-1}(1.9)$
	F_m	$6.00^{+0.12}_{-0.13}$	–	$6.48^{+0.03}_{-0.03}$	$6.57^{+0.05}_{-0.05}$	$5.37^{+0.06}_{-0.07}$

EMCEE MCMC sampler with uniform prior distributions of a_t and b_t and normal prior distribution of $k_t^{\text{prior}} = 0.9 \pm 0.44$. This estimate was obtained by Pushkarev & Kovalev (2015) for the 'core size–frequency' dependence for a large AGN sample and is a reasonable guess in case of a conical non-accelerated jet (e.g. Kutkin et al. 2014 showed that the core size and the time lags follow the same power law in the blazar 3C 454.3).

The parameter $b_t < 0$ d corresponds to the delay between the flare peak at a given highest frequency and 'infinite' frequency, $a_t > 0$ d characterizes the flow speed, and k_t reflects the opacity mechanism. As seen in Fig. 5 the measured peak-to-peak delays differ from one flare to another. Moreover, there are flares with unusual lags when a peak comes earlier at lower frequency (Table 2). Similar unexpected time delays in the source have been reported by Kraus et al. (1999) for a short flare in 1992 that is a part of D-flare in our notation.

We obtain a wide range of parameters $0.7 \le k_t \le 1.8$ with median value $k_t = 1.2$. The posterior k_t distributions are plotted in Fig. 6 for the two marginal cases (D1-flare with $k_t = 1.8$ and F2-flare with $k_t = 0.7$), showing the difference between the k_t values with confidence more than 95 per cent. We find no correlation between k_t and the peak flux density of the flares. The changing of k_t in time is not monotonic.

Different values of the index k_t within one source for separate flares have been also reported by Kudryavtseva et al. (2011). The reason for its change is not obvious, and may be related to the intrinsic changes in the jet, e.g. when the injected particles distort the profile of initial electron distribution in the outflow.

In the last panel of Fig. 5 the light curve of the 37 GHz single-dish flux density is shown along with the 43 GHz light curves of the core and the superluminal component Gc (see also Section 8.2). Peak-to-peak time delay between the component and the core flares obtained using GPR is $T_{\text{Gc,max}} - T_{\text{Core,max}} = 21 \pm 4$ d. One can see, that the total flux density measured by the single-dish telescopes is the sum of the core and Gc and has a maximum somewhere in the middle between their peaks. Therefore, the measured time lags between

the single-dish flares might be biased (i.e. systematically differ from the delay between the moments of passing of a disturbance through the core). The flare profile of the total flux density differs from that of the core since the former is the superposition of the latter and the one of the component Gc. While the rising parts of the profiles are similar, the peak and decay differ: they are smoother for the total flux density profile, as can be seen in the last panel of Fig. 5. Therefore, if a single-dish light curve is used for estimation of brightness temperature and Doppler factor, there might be a bias due to overestimation of the variability time-scale (see also Section 7).

6 CORE SIZE AND SPECTRUM

The frequency dependence of the apparent core size follows power law $W_{\text{core}} \propto \nu^{-k_w}$, where k_w characterizes the opacity mechanism. The index $k_w \approx 1$ when the synchrotron self-absorption dominates, and $k_w \gtrsim 2$ in case of prevailing free–free absorption (e.g. Yang et al. 2009). Pushkarev & Kovalev (2015) found $k_w = 0.90 \pm 0.44$ based on quasi-simultaneous multifrequency observations of a large AGN sample. This value was measured for the sources located at the Galactic latitudes higher than $\sim 10°$. The authors also found $k_w \approx 1.8$ for the Galactic plane residents indicating significant interstellar scattering.

The core in both multifrequency VLBI experiments is well described by the elliptical Gaussian model with the mean axial ratio $\epsilon \sim 0.5$ (see Table 1). The dependence of its major and minor axes [full width at half-maximum (FWHM) of the Gaussian] on frequency is approximated with the model $W(\nu) = a_w \nu^{-k_w}$ (an absence of an additional constant term here suggests that the core has 'zero' size at 'infinite' frequency). Since there is no significant difference between the core size obtained in both VLBI experiments at 5 and 8 GHz, we merge all the data from these experiments for a better fit representation (see Fig. 7).

Both major and minor axes follow the power law with $k_{w,\,\text{maj}} = k_{w,\,\text{min}} = 0.8 \pm 0.1$ ($a_{w,\,\text{maj}} = 1.1 \pm 0.1$,
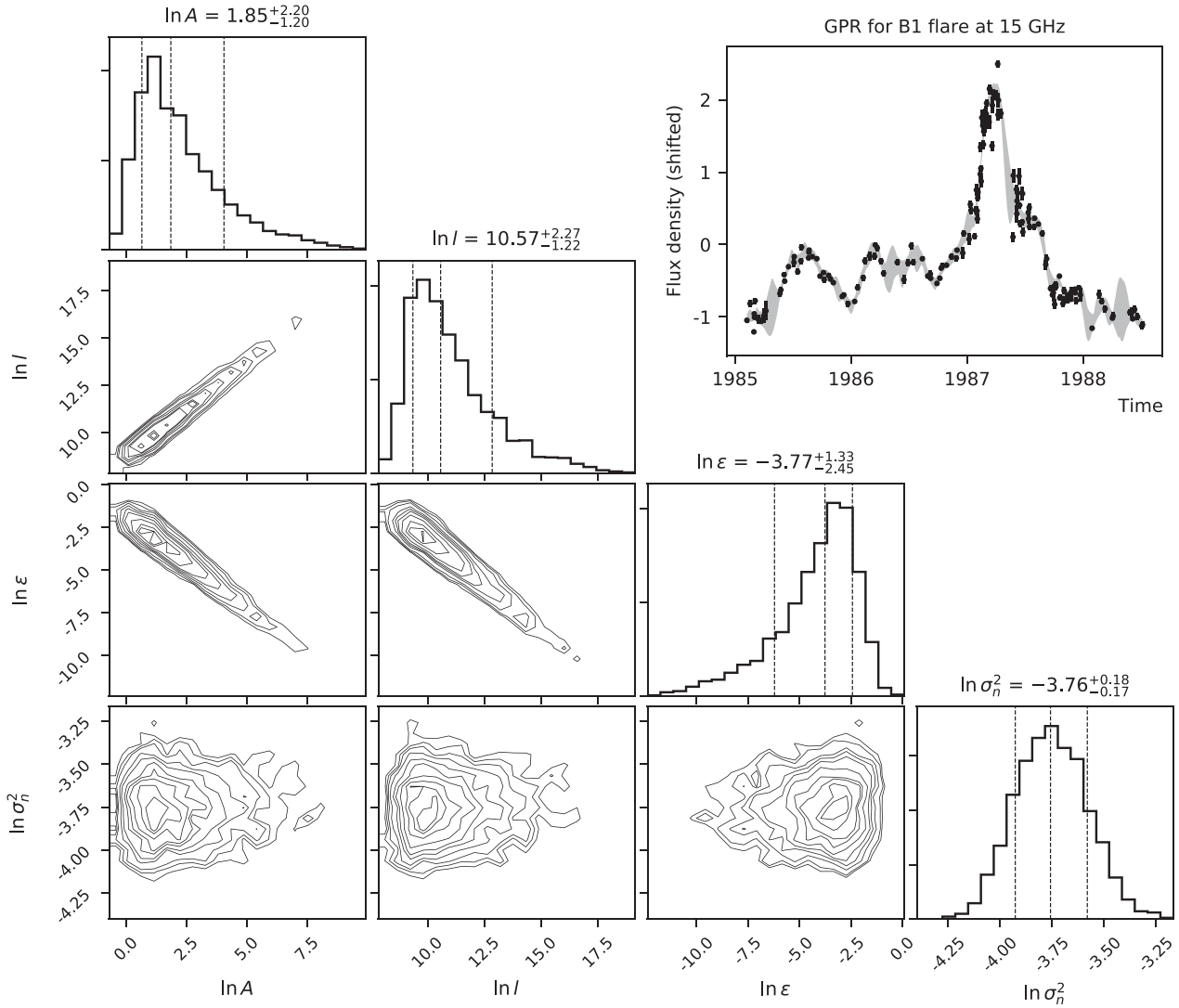
Figure 3. Application of GPR to the 15 GHz B-flare: the posterior distributions of GP hyperparameters (dashed lines indicate 16, 50, and 84 percentiles). The light curve with mean flux density subtracted is shown in the upper right corner, shaded area denotes $\pm 3\sigma$ confidence interval of GPR.
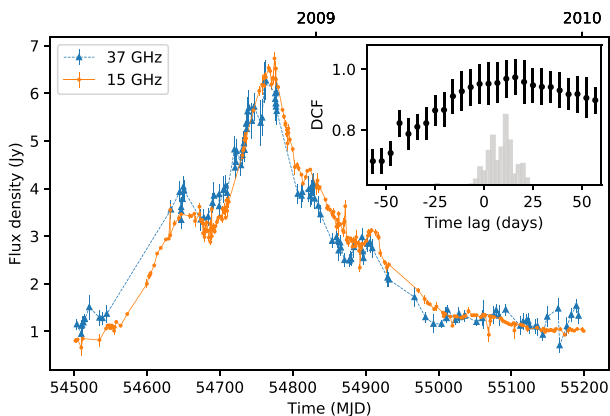
Figure 4. The G-flare at 37 and 15 GHz. Their mutual DCF is shown in the upper right exes. The time lags distribution obtained with FR/RSS simulations are shown with grey bars (not normalized). The resulting marginal time delay is $\Delta T = 12 \pm 8$ d.

$a_{w,\,\mathrm{min}} = 0.65 \pm 0.07$), which is in good agreement with the photosphere scenario. Since the modelled core size at 1.7 GHz does not fulfil the resolution criteria, the upper limit is used. The core at 2.3 GHz is formally resolved, however, its size $W_{\mathrm{maj}} \approx 0.8$ mas is larger than that expected within the synchrotron self-absorption model (~ 0.6 mas). The axial ratio $e > 0.7$ at this band also falls out from the rest data. The interstellar scattering might be significant at these frequencies. For the given celestial position the angular broadening predicted by the NE 2001 model (Cordes & Lazio 2002) is $W_{\mathrm{NE,2.3\,GHz}} = 0.16$ mas, much lower than the core size obtained from modelling. This suggests that if the scattering comes into play here, there is really much denser Galactic medium in that direction, than proposed by the NE 2001 model. We also note, that excluding the data at 1.7 and 2.3 GHz does not affect the results of the fit.

The power-law index found for the core size dependence k_w is measured with accuracy better than k_t and can be used to constrain the model-fit parameters of the time lags dependence for the G-flare (within the assumption of a conical non-accelerated jet). For that purpose we employ the EMCEE sampler with narrow (informative) prior distribution for $k_t = k_w = 0.8 \pm 0.1$ and obtain distributions of the other two parameters, yielding $a_t = 80 \pm 14$ d and $b_t = -3 \pm 2$ d.
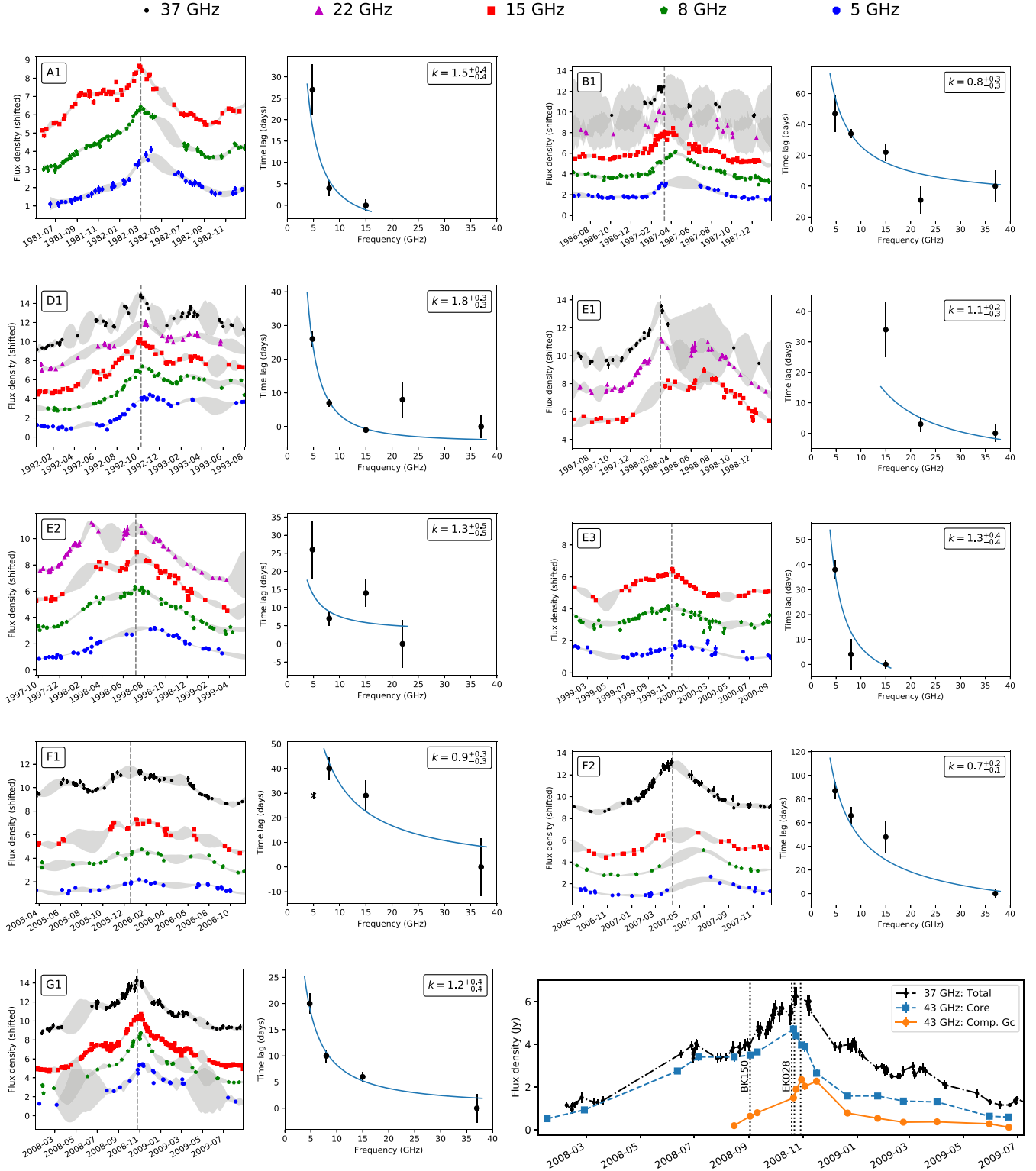
Figure 5. Separate flares and corresponding time lags. Vertical dashed lines mark the peak time at the highest frequency. The grey shaded area corresponds to ±3σ confidence interval of the GPR. The light curves of single-dish 37 GHz, the core, and the component Gc for the G-flare are shown on the last panel (the multifrequency VLBI experiments are marked with vertical dotted lines).

The time lags and the refined model are shown in Fig. 7 (the right axis).

The core spectrum is shown in Fig. 8 for two multifrequency experiments (the core flux density at a given band is assumed to remain constant during each experiment and a possible shift of the core is neglected). The optically thick spectral index increases from $\alpha_1 = 0.39 \pm 0.09$ to $\alpha_2 = 0.64 \pm 0.05$, possibly due to the peak at lower frequencies lagging with respect to higher
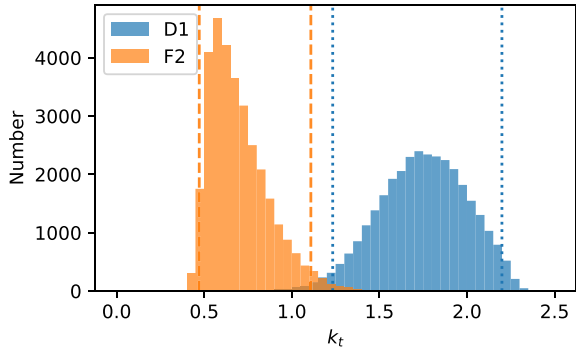
Figure 6. Posterior distributions of k_t parameter for D1 and F2 flares. Vertical dotted and dashed lines denote the 95 per cent intervals, indicating significant difference of k_t.
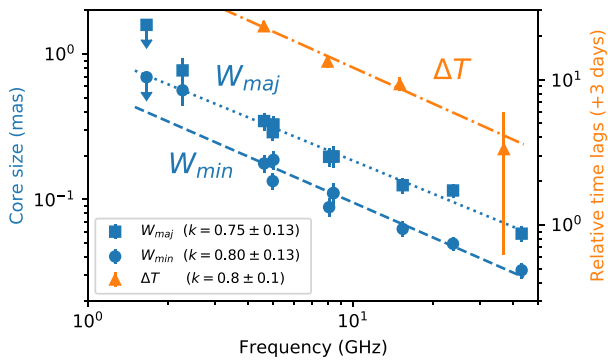
Figure 7. The core size W (left axis) and the time lags of the G-flare peaks ΔT (right axis) versus observations frequency.

frequencies. We also discuss possible influence of adiabatic losses in Section 9.

7 BRIGHTNESS TEMPERATURE AND DOPPLER FACTOR

7.1 Ground-based data

The apparent brightness temperature of a jet component in the source frame can be estimated using the model parameters (e.g. Kovalev et al. 2005):

$$T_{\rm b} = 1.22 \times 10^{12}\,{\rm K}\, \frac{S/{\rm Jy}\,(1+z)}{(\nu/{\rm GHz})^2\, W_{\rm maj}/{\rm mas}\, W_{\rm min}/{\rm mas}}, \qquad (5)$$

where S is the flux density, $W_{\rm maj}$ and $W_{\rm min}$ are the major and minor apparent size (FWHM of a Gaussian model), z is the redshift, and ν is the observing frequency.

On the other hand it is possible to estimate the so-called variability brightness temperature in the source frame assuming that the variability time-scale $t_{\rm var}$ corresponds to the light-crossing time of the component size (e.g. Hovatta et al. 2009):

$$T_{\rm b,var} = 1.05 \times 10^8\,{\rm K}\, \frac{(D_\ell/{\rm Mpc})^2\, S_{\rm obs}/{\rm Jy}}{(1+z)(\nu/{\rm GHz})^2(t_{\rm var}/{\rm yr})^2}, \qquad (6)$$

where D_ℓ is the luminosity distance, $S_{\rm obs}$ is the flux density, ν is the observations frequency, and $t_{\rm var}$ is the variability time-scale.
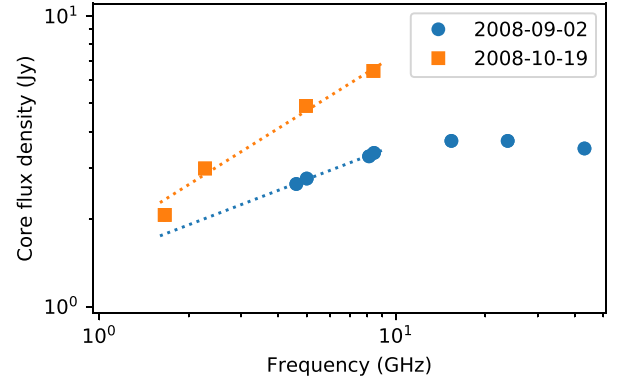
Figure 8. The core spectra for two epochs during the flare measured from VLBA and EVN data.

$T_{\rm b}$ and $T_{\rm var}$ are measured experimentally and can be expressed through an intrinsic brightness temperature $T_{\rm int}$, amplified by Doppler boosting (e.g. Kellermann et al. 2007):

$$\begin{cases} T_{\rm b} = \delta T_{\rm int} \\ T_{\rm b,var} = \delta^3 T_{\rm int}, \end{cases} \qquad (7)$$

where δ is the Doppler factor. From equation (7) we obtain δ and $T_{\rm int}$.

We adopt the following parameters: $D_\ell = 6142\,{\rm Mpc}$, $z = 0.94$, $S_{\rm obs} = 4.7\,{\rm Jy}$ – peak value of the core flux density during the G-flare, and $t_{\rm var} = 0.09\,{\rm yr}$ – time-scale of the core variability during the flare. Note, that the flare profile has a plateau and differs from the two-sided exponential. Moreover, the flare decays faster than it rises. We estimate the scale using the time interval and flux density change between the observations i, j as $t_{\rm var} = |(t_i - t_j)/\ln(S_i/S_j)|$. The shortest time-scale is the pairs (i, j) falls on the flare decay (epoch 2008-11-03). Thus, we use a self-consistent system to estimate Doppler factor and intrinsic brightness temperature, considering the size and variability time-scale of the same region (the core).

We obtain $T_{\rm b,var} = 6.4 \times 10^{14}\,{\rm K}$ and $T_{\rm b} = 1.5 \times 10^{12}\,{\rm K}$, which yields $\delta \approx 21$, and $T_{\rm int} \approx 7 \times 10^{10}\,{\rm K}$. This value is close to the equipartition brightness temperature $T_{\rm eq} \simeq 5 \times 10^{10}\,{\rm K}$, suggested by Readhead (1994).
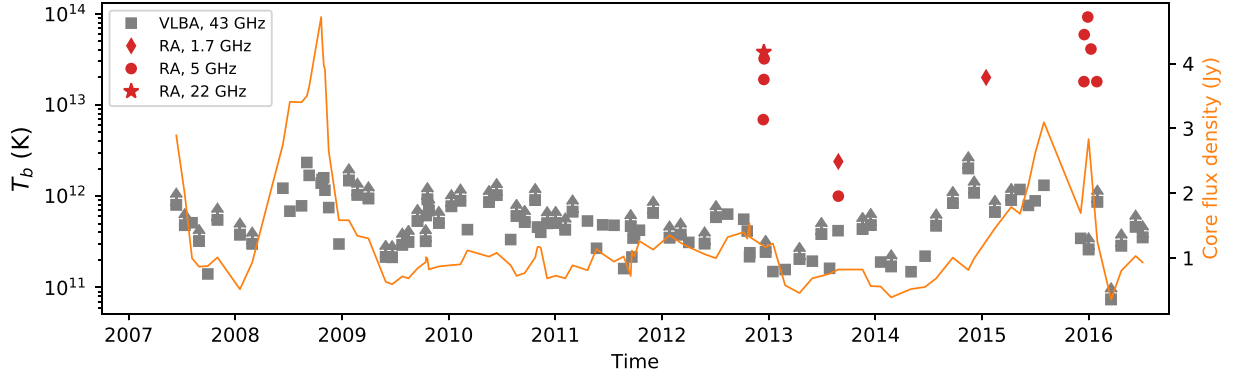
We also estimate the apparent brightness temperature for each VLBA observation at 43 GHz. These measurements are plotted with grey squares in Fig. 9 (arrows indicate the lower limits of $T_{\rm b}$ in cases of unresolved core). Note that during the flares (2008 and 2015) the apparent brightness temperature increases by a factor of about 2.

7.2 The *RadioAstron* data

We estimate a lower limit of apparent brightness temperature $T_{\rm b}^{\rm min}$ in the source frame assuming that the brightness distribution has a circular Gaussian profile (Lobanov 2015):

$$T_{\rm b}^{\rm min} = \frac{\pi e}{2k_{\rm B}} L^2 V_L \approx 3.09\,{\rm K}\left(\frac{L}{\rm km}\right)^2\left(\frac{V_L}{\rm mJy}\right)(1+z), \qquad (8)$$

where $k_{\rm B}$ is the Boltzmann constant, L is the projected baseline, V_L is the visibility amplitude measured on that baseline. Uncertainty of the visibility amplitude is estimated from the statistical (thermal) noise of data as well as amplitude calibration errors. For the latter we adopt the typical 10 per cent value (Kovalev et al. 2014). $T_{\rm b}^{\rm min}$ must be considered as the most conservative limit, which can be achieved for the given visibility amplitude. Further, we derive the size W from modelling visibility amplitudes on ground–ground and

Figure 9. The apparent brightness temperature by VLBA at 43 GHz and *RadioAstron* at 1.7, 5 and 22 GHz. Arrows mark T_b estimated using the resolution limits. The curve shows core flux density at 43 GHz (right axis).

Table 3. *RadioAstron* observations of 0235+164. Columns: (1) date, (2) band, (3) projected baseline (in Earth diameters), (4) lower limit of brightness temperature, (5) estimate of the apparent brightness temperature in the source frame, (6) estimate of circular Gaussian component size.

Date	ν	$D/D_\oplus$	T_b^{min}	T_b^{Gaus}	W
	(GHz)		(K)	(K)	(μas)
(1)	(2)	(3)	(4)	(5)	(6)
2012-12-13	5	7.7	3.6×10^{12}	6.9×10^{12}	111.8
2012-12-15	5	14.9	3.8×10^{12}	1.9×10^{13}	71.4
2012-12-15	22	14.8	1.6×10^{13}	3.8×10^{13}	13.3
2012-12-16	5	18.7	8.4×10^{12}	3.2×10^{13}	54.4
2013-08-27	5	2.2	6.9×10^{11}	1.0×10^{12}	376.2
2013-08-27	1.7	2.8	2.3×10^{12}	2.4×10^{12}	457.3
2015-01-15	1.7	19.8	2.9×10^{12}	2.0×10^{13}	164.4
2015-12-16	5	8.7	1.1×10^{13}	1.8×10^{13}	95.7
2015-12-17	5	16.4	1.4×10^{13}	5.9×10^{13}	63.1
2015-12-29	5	25.5	1.4×10^{13}	9.2×10^{13}	43.3
2016-01-09	5	14.5	1.8×10^{13}	4.1×10^{13}	62.0
2016-01-29	5	8.9	6.4×10^{12}	1.8×10^{13}	104.6

ground–space baselines with a circular Gaussian profile and estimate the corresponding brightness temperature T_b^{Gaus} (see equations 1 and 2 in Lobanov 2015). We note that T_b^{Gaus} might also be treated as a less strict lower limit, since the real component size cannot exceed the estimate W (see below). The lower limit T_b^{min}, the estimate T_b^{Gaus} and the size W are shown in columns 5 and 6 in Table 3.

The highest brightness temperature estimate comes from the fringe detection on the baseline 26 Earth diameters at 5 GHz. The longest baseline in units of wavelengths is 14 Gλ achieved at 22 GHz. The average apparent brightness temperature measured by *RadioAstron* is about an order of magnitude higher than that measured by VLBA (Fig. 9). The estimates T_b^{Gaus} and even conservative lower limit values T_b^{min} do challenge the inverse Compton limit even after correction for boosting by the high value of $\delta \approx 20$.

The size estimates W at 5 GHz are shown in Fig. 10. The core size obtained from modelling of the 5 GHz VLBA data is also shown with the grey square. There is a plateau of the apparent source size on baselines less than about two Earth diameters, suggesting the presence of two scales in the inner compact source structure. The first one is the 'core'. It is resolved by ground-based VLBI and has intrinsic brightness temperature close to the equipartition value (see the previous section), which can be considered as an average value over the whole core region. The second is ultra-compact, less than about 10 μas or 0.1 pc, which remains unresolved even on the longest ground–space projected spacings. The brightness tempera-
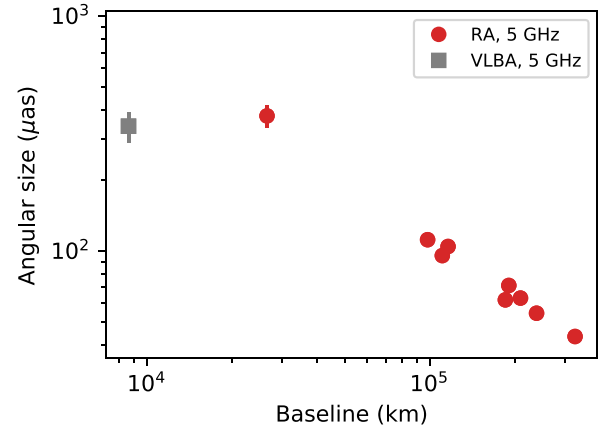

Figure 10. The source angular size estimated by fitting *RadioAstron* visibility amplitudes at 5 GHz (circles, Table 3). The square marks the size of the core at 5 GHz from ground-based VLBA measurements (Table 1).
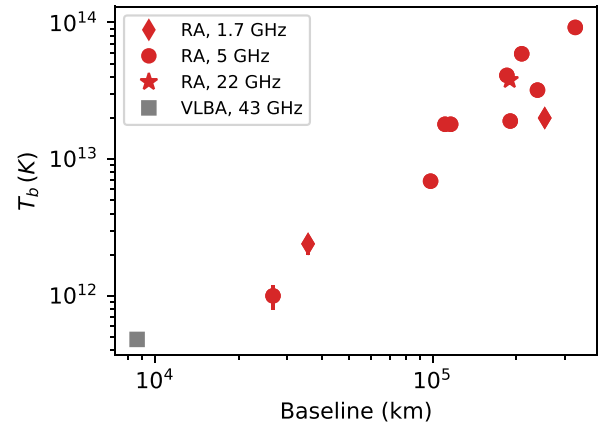
Figure 11. The apparent brightness temperature T_b^{Gaus} measured by *RadioAstron* versus the baseline (Table 3). Diamonds, circles, and the star represent T_b measured at 1.7, 5, and 22 GHz, respectively. The square marks median T_b measured by 43 GHz VLBA.

ture, T_b^{Gaus}, measurements by *RadioAstron* and VLBA are plotted against projected baseline in Fig. 11. These estimates increase with projected baseline (see also Fig. 10 for the corresponding angular size dependence) which is a clear indication of a lower limit behaviour. We conclude that the angular size values from Fig. 10 and
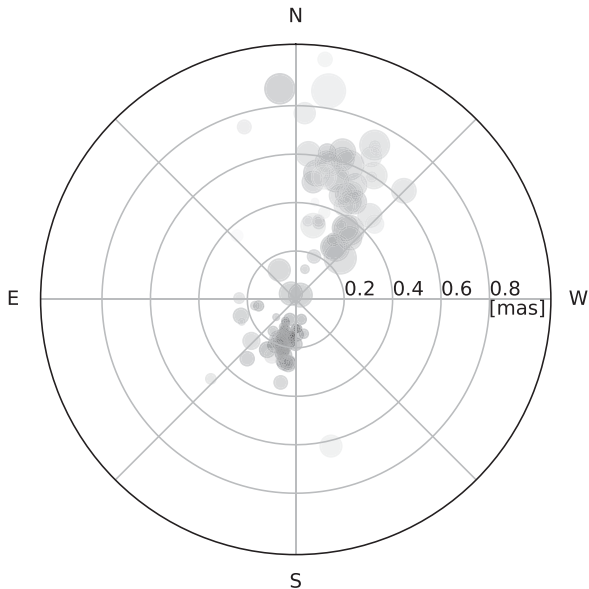
Figure 12. The model components within 1 mas of the core, aligned relative to the position of the core (not plotted). The circles size and colour intensity are proportional to the size and flux density of the components, respectively.
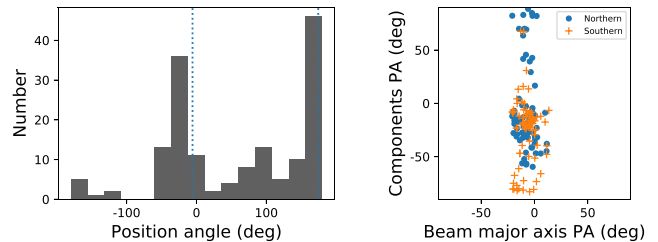

Figure 13. *Left:* the distribution of the components PA (vertical lines show the median of the beam major axis orientation). *Right:* the components PA reduced to $[-90°, 90°]$ versus the PA of the beam major axis.

**Figure 14.** The size of components versus their distance from the core.

the brightness temperature values from Fig. 11 should be considered as upper and lower limits, correspondingly.

The high brightness temperatures measured by *RadioAstron* in 0235+164 can be associated with an extremely compact (<10 μas) feature in the jet of the source. It might be related to shocks or plasma blobs crossing the photosphere, e.g. through a tiny spine. One can see that generally the measured brightness temperatures are higher when the source is in a flaring state (Fig. 9). However, the high values appear during the quiescent states as well. Therefore, the bright compact features occur in the jet without a prominent flare and their relation to the parsec-scale VLBI components (which are usually associated with the outbursts) is not clear.

Rickett et al. (2006) have performed a comprehensive analysis of ISS in 0235+164. They indirectly estimated the size and flux density of an ultra-compact jet feature for 1992–1993 epochs and reported similar values. The authors found the increase of ISS amplitude during two major outbursts in the source (C and D in our notation) and suggest that the compact features might be associated with the new-born jet components. They travel down the jet and expand. The ISS of such a component has enough amplitude to produce the variability brightness temperatures up to $\sim 10^{14}$ K at frequencies 2–8 GHz (Rickett et al. 2006).

Interstellar scattering sub-structure (e.g. Johnson et al. 2016) of these features, in principle, might lead to the observed values of brightness temperature at cm-wavelengths. However, it does not seem to play significant role in the observed source structure at 22 GHz (see for details Johnson & Gwinn 2015). Therefore, the values of $T_b > 10^{13}$ K should have an intrinsic nature. We note that simultaneous measurements of T_b^{Gaus} at 5 and 22 GHz on 2012-12-15 (Table 3) result in similar brightness temperature values providing an additional argument in favour of intrinsic scenario even at 5 GHz.

We find some clues to the presence of very fast bulk flow speed in the source (see Section 9). Possibly, there are regions with velocity gradients, like a spine-sheath structure of M87 (e.g. Mertens et al. 2016). The higher flow speed in the spine could yield the higher Doppler boosting. Moreover, such a spine would be a supply chan-

nel of the high-energy electrons, which can partially compensate the inverse Compton cooling (see e.g. Readhead 1994). Then the high brightness level might persist in the source for a long time. Kovalev et al. (2016) discuss other possible explanations of the ultra-high apparent brightness temperatures, e.g. the synchrotron emission from relativistic protons, mono-energetic spectrum of particles, etc. However, they have significant difficulties in explaining the observational data.
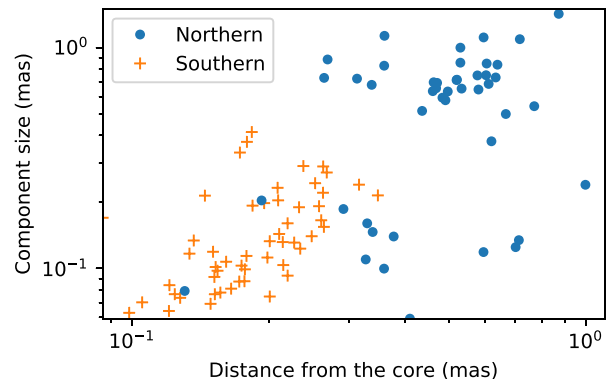
8 JET STRUCTURE

8.1 Image stacking

Due to the faint extended structure of 0235+164 it is difficult to determine jet geometrical characteristics from a single VLBI observation. Moreover, even the direction of the jet is not clear. In Fig. 12 all our models of the 100 43 GHz VLBA observations are plotted with respect to the core position (the core is not shown). It is clearly seen that the components tend to concentrate almost symmetrically in two directions. We checked if the position angles (PA) of the components (median $-28°$ and $162°$) correlate with the major axis of the synthesized beam (median $-6°$). They are found to be close but we did not find the correlation between them (Fig. 13). Therefore, the beam orientation does not seem to be responsible for the observed phenomena. Another support for the components PA indicating the jet PA comes from the fact that the size of the components increases with distance from the core both in southern and northern directions. Moreover, in the northern part the components are more distant and larger on average (see Fig. 14). We interpret this as a bend of the outflow from south to north, so that the younger (closer to the central engine) jet is observed southwards and the older (more extended and prominent) is seen northwards of the core.
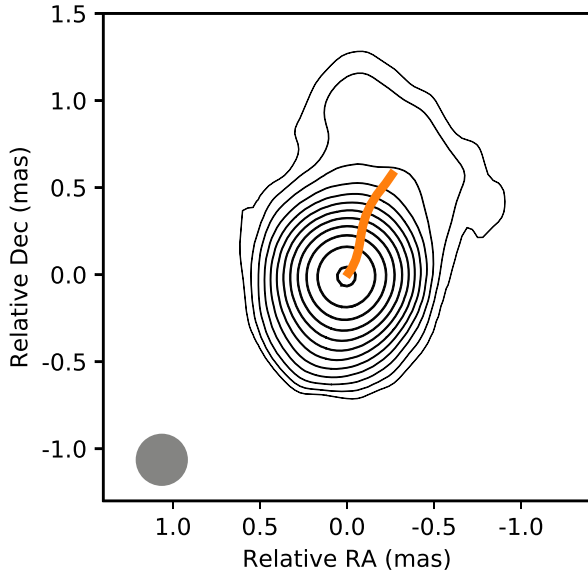
Figure 15. The stacked map of 0235+164 at 43 GHz. Thick curve shows the ridgeline. Grey circle in the lower left corner shows the beam at FWHM level. The contours of equal intensity are shown at x2 steps. The first contour is 0.6 mJy beam^{-1}, the peak is 1.5 Jy beam^{-1}, the RMS is 0.1 mJy beam^{-1}.
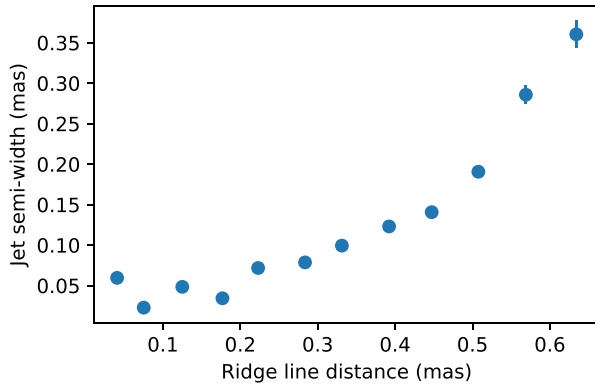
Figure 16. Jet half-width versus distance along the ridgeline.

We combine a hundred of 43 GHz VLBA maps (obtained in independent experiments) aligned by the core position into a stacked image to increase dynamic range. For all the images we use the same circular beam of 0.3 mas at FWHM level. This procedure allows us to detect the jet and to construct the ridgeline towards north-north-west of the core as shown in Fig. 15. The jet to the south of the core is very compact and the corresponding ridgeline is too short to perform calculations. The intensity along transverse jet slices measured down the ridgeline is fitted with a Gaussian profile. The jet width w is then found as a deconvolution of the obtained Gaussian with the beam. The apparent opening angle φ is estimated as $\varphi = 2 \arctan(w/2l)$, where l is the distance along the ridgeline. The jet profile ($w/2$ versus l) is shown in Fig. 16. At the ridgeline distance longer than 0.7 mas the jet width estimate becomes uncertain due to low signal-to-noise ratio. Assuming conical geometry we find $\varphi_{43} = 60° \pm 5°$. It is twice as large as the value obtained by Pushkarev et al. (2017) for stacked 15 GHz image ($\varphi_{15} = 30°$ on scales $\gtrsim 1.5$ mas). At 43 GHz we observe the jet much closer to its apex, than at 15 GHz due to synchrotron self-absorption. Hence, we come to the conclusion that the flow is collimated within
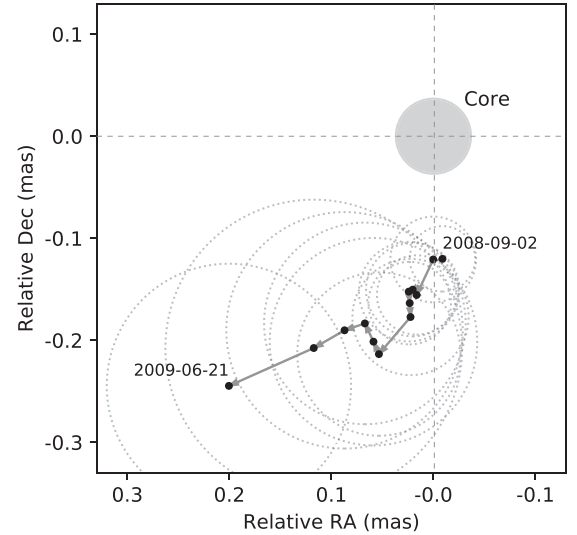
~1.5 mas of the apex. At lower frequency (1.4 GHz, tens mas) the VLBA stacked image shows that the jet changes its direction to north-north-east (Pushkarev et al. 2017) keeping the opening angle ~30°.
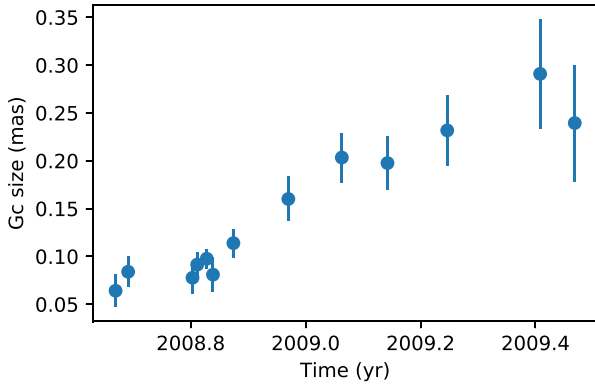
We note, however, that the above jet morphology is not the only one consistent with the data presented. The absence of jet morphology clearly visible in the image plane is consistent with a generic model of a blazar with the direction of the jet outflow very close to the direction to the observer. If such a geometry is considered in combination with the assumption that what is perceived as the core is actually a blend of a true core and a bright new variable (e.g. quickly fading) component, then the centroid of that assumed core would shift and produce apparent 'wobbling' of the jet in opposite directions. Further ingredients contributing into this morphology might include a helical jet, e.g. as in the well-studied case of the blazar 1156+295 (Hong et al. 2004; Zhao et al. 2011). In particular, the jets conical helicity with a varying pitch might explain the distribution of bright components by position angle relative to the core shown in Fig. 12. Within the framework of this model, the jet components appearing on the opposite sides from the core would be at different spirals of the helical trajectory.
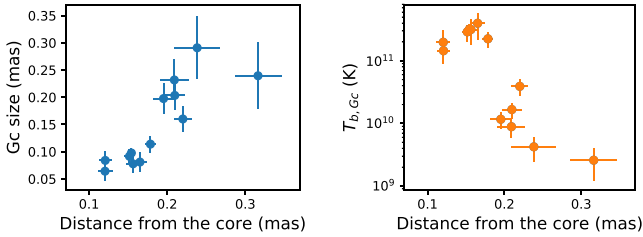
8.2 Gc component

The G-flare (see Fig. 2) is accompanied by a bright feature (Gc hereafter) located to the south-south-east from the core and travelling with apparent superluminal velocity (see below). It has been also studied by Agudo et al. (2011), who interpreted it as a moving transverse shock.

In Fig. 17 the trajectory of Gc is shown relative to the core position. The mean proper motion of Gc relative to the core is $\mu = 0.20 \pm 0.03$ mas yr^{-1}, which corresponds to an apparent speed $\beta_{app} = 10 \pm 1.6\,c$. The position and speed of Gc is consistent with its ejection in 2008 January, at the beginning of the core (and total flux) flare.

Using equations (5)–(7) we estimate the brightness temperature and Doppler factor of Gc. During the flare peak $T_{b,\,Gc} \approx 4 \times 10^{11}$ K

Figure 17. Trajectory of the Gc component during 2008 September–2009 June at 43 GHz. Dots, arrows and open circles show the position, path, and size of the Gc. The core is at (0,0) and its median major axis shown with grey circle.

Figure 18. The size of the component Gc versus time.

Figure 19. The size and apparent brightness temperature of Gc versus its separation from the core.

(Fig. 19). Taking the variability time-scale at Gc-flare peak $t_{\text{var, Gc}} = 0.1$ yr (estimated in the same way as for the core at flare decay in 2008 November) and corresponding $T_{\text{var,Gc}} = 2.4 \times 10^{14}$ K we obtain $T_{\text{b,int,Gc}} \approx 10^{10}$ K and $\delta_{\text{Gc}} \approx 24$.

The Lorentz factor and the viewing angle can be estimated using the following equations:

$$\Gamma = \frac{\beta_{\text{app}}^2 + \delta^2 + 1}{2\delta}, \quad \theta = \arctan \frac{2\beta_{\text{app}}}{\beta_{\text{app}}^2 + \delta^2 - 1}, \quad (9)$$

which give $\Gamma \approx 14$ and $\theta \approx 1.7°$.

The slope of Gc size versus distance from the core is 1.2 ± 0.4 implying the conical angle $\varphi_{\text{Gc}} \approx 62°$ is consistent with the opening angle φ obtained from the stacked image in the northern jet. Therefore, the Gc component occupies the whole jet cross-section, supporting the bent-jet scenario. The intrinsic opening angle of the jet is then $\varphi_{\text{int}} = \varphi_{\text{Gc}} \sin \theta \approx 2°$.

If the viewing angle of the inner jet (in the core region) is the same as of Gc, then the Lorentz factor and apparent speed in that region are also kept as $\delta_{\text{core}} \approx \delta_{\text{Gc}}$.

We come to the conclusion that the component Gc is the true physical part of the jet of 0235+164, rather than an artefact of calibrations. This is strongly supported by the evolution of its size and brightness temperature with time and distance from the core (Figs 18 and 19) as well as by its birth date. Moreover, since the component fits the width of the outflow, its trajectory depicts the form of the jet.

Jorstad et al. (2017) recently published the `Difmap` models of 0235+164 for 2007–2013 period based on the same data at 43 GHz. The authors reported three components B1, B2, and B3 in the jet with estimated birth epochs 2007.4, 2008.3, and 2008.8, respectively. All of the features were found to have different velocities in different directions. The key difference between the aforementioned

models and that obtained in this work is that we used elliptical Gaussian core based on the cross-validation. If the core has an elliptical form and circular model is used, one would typically obtain more than one very close and compact model-fit components. Some of them usually remain unresolved and have low flux density. These features needlessly complicate a model. We performed a brief comparison of the core flux density and size [$(W_{\text{maj}} * W_{\text{min}})^{1/2}$] derived in this work and that by Jorstad et al. (2017) and found good agreement of these parameters over all the period 2007–2013. We also used cross-validation to compare the models for 2008-08-15 observations epoch, where the core parameters mostly differ. The resulting cross-validation scores for the models are consistent within errors. At the same time model with elliptical core is simpler (two components) and hence is more preferable. We also note, that the same data were studied previously by Agudo et al. (2011), who reported the single component in the jet of 0235+164 during 2008–2009.

9 CORE SHIFT AND PHYSICAL PARAMETERS

Due to the extreme compactness of the source the core shift cannot be measured using optically thin jet features. However, it can be estimated indirectly based on the parameters derived above. The apparent core shift Δr and change of its transverse size ΔW_{min} as a function of frequency in a conical jet are related through the apparent opening angle φ as $\Delta r = \Delta W_{\text{min}}/2 \tan \varphi/2$. Here, we assume that major and minor core axes are aligned with axial and transverse directions of the inner jet, which is typical for blazars (Kovalev et al. 2005).

Then it is easy to estimate the expected core shift for a given frequency pair. For example, the shift between the core at 15 and 8 GHz is $\Delta r_{15-8} \approx 0.03$ mas, which is several times lower than the median value (0.128 mas) obtained by Pushkarev et al. (2012) at these frequencies. The smaller core shift value is expected for a source having a small viewing angle. The core shift between 15 GHz and 5 GHz should be $\Delta r_{15-5} \approx 0.1$ mas.

Consider the standard scalings for the particle density $N = N_1(r/r_1)^{-n}$ and the magnetic field strength $B = B_1(r/r_1)^{-m}$, where index 1 refers to values at 1 pc from the central engine. In a freely expanding jet (without ambient-medium pressure) the power-law indices m, n can be linked through the index k (the conical geometry implies that the core shift index k equals to k_w measured in Section 6) and the optically thin spectral index α (Konigl 1981)[8]:

$$k = \frac{5 - 2\alpha}{(3 - 2\alpha)m + 2n - 2} \quad (10)$$

Further we discuss the equipartition regime, when the energy density of relativistic electrons roughly equals to that of the magnetic field. We also consider another scenario, where the conical jet undergoes adiabatic losses.

9.1 Equipartition case

Estimation of physical parameters can be performed taking into account the fact that the intrinsic brightness temperature of the core is close to the equipartition value $T_{\text{b,eq}} \sim 10^{10.5}$ K. The equipartition between particles and magnetic field energy density implies that $n = 2m$, and from (10) for $k = 0.8 \pm 0.1$, $\alpha = -0.5$ we obtain $m = 1.2 \pm 0.1$ and $n = 2.4 \pm 0.2$. Note, that the dependence of the

---

[8] Note, that throughout this paper k is defined as Königl's k_r^{-1}.

parameters on α is weak, and using $\alpha = -0.75$ changes the above results insignificantly.

The measure of core offset for a given frequency pair ν_1, ν_2 can be introduced following Lobanov (1998):

$$\Omega = 4.85 \times 10^{-9} \frac{\Delta r_{\mathrm{mas}} D_\ell}{(1+z)^2} \left(\frac{\nu_1^k \nu_2^k}{\nu_2^k - \nu_1^k} \right), \qquad (11)$$

where D_ℓ is the luminosity distance in pc, Δr_{mas} is the core shift in mas. Then magnetic field strength at 1 pc:

$$B_1 \approx 0.025\,\mathrm{G} \left(\frac{\Omega^{3/k}(1+z)^2}{\delta^2 \phi \sin^{3/k-1}\theta} \right)^{1/4}, \qquad (12)$$

where θ is the jet viewing angle, ϕ is the jet half opening angle, and δ is the Doppler factor. Substitution of the parameters gives $B_1 \approx 1.3\,\mathrm{G}$. The de-projected distance from the central engine to the core at a frequency ν is then

$$r_{\mathrm{core}}(\nu) = \frac{\Omega}{\sin\theta} \nu^{-k} \;(\mathrm{pc}). \qquad (13)$$

For example, the core at 43 GHz is located at $r_{\mathrm{core},\,43} \approx 10.5$ pc, while the core at 2.3 GHz is more than 100 pc downstream from the jet apex. The magnetic field in the 43 GHz core is $B_{43,\,\mathrm{core}} \approx 0.1$ G, which is typical for blazars (e.g. Sokolovsky et al. 2011; Pushkarev et al. 2012; Kutkin et al. 2014; Lisakov et al. 2017).

9.2 Adiabatic case

The inverted spectrum of the core at lower frequencies (Fig. 8) may also be related to the adiabatic losses, which might dominate in the jet on parsec scales (Marscher 1980). Let $m = 1$, as expected for the transverse magnetic field (Blandford & Rees 1974), and $n = 2/3(2 - s)$, where s is the slope of the electron energy distribution's power law. The optically thin spectral index is $\alpha = (s + 1)/2$. Then the solution of equation (10) gives $s = -2.15$. This value is very close to that predicted by models of electron acceleration by relativistic shocks in AGN jets (Kirk et al. 2000). Note, that the dependence of s on the observed index k is very strong, e.g. changing k from 0.7 to 0.9 changes s from -3.4 to -1.5. If we assume $m = 2$ instead (the longitudinal magnetic field), we obtain unrealistic slope $s(k = 0.8) = -0.16$.

Therefore, both equipartition and adiabatic cases suggest m close to 1, and reject $m = 2$, implying the dominance of the transverse component of the magnetic field in the parsec-scale jet.

9.3 Jet speed

In Section 8.2 we estimate the apparent speed of the superluminal component. The obtained value is typical among the velocities derived from kinematics of the moving features in the jets of luminous blazars (see e.g. fig. 10 by Kellermann et al. 2007). There is yet another method to estimate apparent speed of a jet at its innermost parts (in the core region).

It is natural to assume that the peak of a flare at a given frequency occurs when a disturbance travelling downstream the jet crosses the core at this frequency. Then the apparent core shift can be expressed through the time delay as $\Delta r = \mu \Delta T$, where μ is the proper motion of the bulk flow in the core region. For $\Delta r_{15-5} = 0.1$ mas and $\Delta T_{\mathrm{G},\,15-5} = 14$ d we obtain $\mu = 2.6$ mas yr^{-1} ($130\,c$ at the source redshift), which is an order of magnitude higher than the proper motion of the Gc jet component. Therefore, the bulk flow speed is much higher than the pattern speed in the source outflow. Similar result was obtained for the blazar 3C 454.3 by Kutkin et al. (2014).

The observed extreme brightness temperatures of the innermost jet regions may be attributed to the ultra-high bulk flow speed. We note, however, that the core shift of 0235+164 is estimated indirectly, and might be a subject of concern. In any case, this question must be studied further by direct core shift and time delays measurements of more blazars.

10 SUMMARY

We study the frequency dependence of peak-to-peak time delays of the outbursts in the blazar AO 0235+164. In parallel, we analyse the frequency dependence of the apparent size of the radio core in the source. Our results support the dominance of synchrotron self-absorption in the jet at cm-wavelengths. We implement a self-consistent method to estimate Doppler factor and intrinsic brightness temperature of the core using the size and variability scale of the same region. The resulting value of $T_{\mathrm{b,int}}$ is close to that expected in the equipartition regime.

The brightness temperature measured using ground-based VLBI increases by a factor of about 2 during the flares, but still is much lower than that obtained with the ground–space radio interferometer *RadioAstron*, where visibility amplitudes of 50–100 mJy are detected on baselines up to 14 Gλ. We find evidence for the presence of ultra-compact, less than 10 μas or 0.1 pc, features in the source. They might demonstrate fast flux density variations at cm-wavelengths via the ISS mechanism, in good agreement with the observed intra-day variability of 0235+164. The recently discovered scattering sub-structure is not expected to appear at least at 22 GHz therefore the extreme brightness of the source up to 10^{14} K might have intrinsic nature, and is possibly related to regions of ultra-high bulk flow speed in the inner jet. The signature of high speed in the jet base also comes from the comparison of the derived core shift and the corresponding peak-to-peak time delay at frequencies 5 and 15 GHz for the flare in 2008.

There is a superluminal jet feature in the source seen on 43 GHz maps during the flare. The estimated birth epoch as well as the increase of its size with time and distance from the core support the conclusion that it is real jet component. The Doppler factor of the component estimated from its kinematic analysis is in good agreement with that found for the core. The two prevalent directions in the spread of the components at 43 GHz are probably caused by jet bending from south to north at about 0.3 mas from the core. The brighter, more compact components are observed closer to the core in the southern jet during all the period studied, which provides strong support for this scenario. The estimates of the opening angle of the southern (from the component size) and the northern (from the stacked image) jet also suggest that its direction changes. Millimetre interferometric observations with higher resolution in the north–south direction would shed more light on this structure. Our estimates of the opening angle, compared to the previously reported, suggest the collimation of the outflow within 1.5 mas of the central engine. Inside this region the intrinsic opening angle of the jet cone is close to the viewing angle, yielding the additional dispersion of position angles of the observed components. We estimate high, but not extreme values of the Lorentz factor $\Gamma = 14$ and the Doppler factor $\delta = 21$, and viewing angle $\theta = 1.7°$.

Based on the derived jet geometry we estimate the expected core shift in the jet of 0235+164. There is evidence that the bulk plasma speed is an order of magnitude higher than the pattern speed in the jet. We consider the equipartition and adiabatic scenarios, which adequately describe the observational data. Both cases imply the dominance of a transverse magnetic field component. We also

derive the gradients of magnetic field strength and electron density in the jet, as well as the distance from the jet apex to the core at each frequency.

[9] http://www.bu.edu/blazars/VLBAproject.html

REFERENCES

Abraham R. G., Crawford C. S., Merrifield M. R., Hutchings J. B., McHardy I. M., 1993, ApJ, 415, 101
Ackermann M. et al., 2012, ApJ, 751, 159
Agudo I. et al., 2011, ApJ, 735, L10
Altschuler D. R., Gurvits L. I., Alef W., Dennison B., Graham D., Trotter A. S., Carson J. E., 1995, A&AS, 114, 197
Ambikasaran S., Foreman-Mackey D., Greengard L., Hogg D. W., O'Neil M., 2015, IEEE Trans. Pattern Anal. Mach. Intell., 38, 2
Blandford R. D., Königl A., 1979, ApJ, 232, 34
Blandford R. D., Rees M. J., 1974, MNRAS, 169, 395
Burbidge E. M., Beaver E. A., Cohen R. D., Junkkarinen V. T., Lyons R. W., 1996, AJ, 112, 2533
Chu H. S., Baath L. B., Rantakyroe F. T., Zhang F. J., Nicholson G., 1996, A&A, 307, 15
Cohen R. D., Smith H. E., Junkkarinen V. T., Burbidge E. M., 1987, ApJ, 318, 577
Cordes J. M., Lazio T. J. W., 2002, preprint (arXiv:astro-ph/e-prints)
Edelson R. A., Krolik J. H., 1988, ApJ, 333, 646
Fomalont E. B., 1999, in Taylor G. B., Carilli C. L., Perley R. A., eds, ASP Conf. Ser. Vol. 180, Synthesis Imaging in Radio Astronomy II. Astron. Soc. Pac., San Francisco, p. 301
Foreman-Mackey D., 2016, J. Open Source Softw., 24. Available at: http://dx.doi.org/10.5281/zenodo.45906
Foreman-Mackey D., Hogg D. W., Lang D., Goodman J., 2013, PASP, 125, 306
Frey S. et al., 2000, PASJ, 52, 975
Gabuzda D. C., Cawthorne T. V., 2000, MNRAS, 319, 1056
Greisen E. W., 1990, in Longo G., Sedmak G., eds, The Astronomical Image Processing System. Acquisition, Processing and Archiving of Astronomical Images. p. 125
Hada K., Doi A., Kino M., Nagai H., Hagiwara Y., Kawaguchi N., 2011, Nature, 477, 185
Hastie T., Tibshirani R., Friedman J., 2009, The Elements of Statistical Learning: Data Mining, Inference, and Prediction, 2nd edn. Springer, Berlin. Available at: http://web.stanford.edu/hastie/ElemStatLearn
Hirotani K., 2005, ApJ, 619, 73
Högbom J. A., 1974, A&AS, 15, 417
Hong X. Y. et al., 2004, A&A, 417, 887
Hovatta T., Valtaoja E., Tornikoski M., Lähteenmäki A., 2009, A&A, 494, 527
Johnson M. D., Gwinn C. R., 2015, ApJ, 805, 180
Johnson M. D. et al., 2016, ApJ, 820, L10
Jones D. L., Baath L. B., Davis M. M., Unwin S. C., 1984, ApJ, 284, 60
Jorstad S. G., Marscher A. P., Mattox J. R., Wehrle A. E., Bloom S. D., Yurchenko A. V., 2001, ApJS, 134, 181
Jorstad S. G. et al., 2017, ApJ, 846, 98
Karamanavis V. et al., 2016, A&A, 590, A48
Kardashev N. S. et al., 2013, Astron. Rep., 57, 153
Keimpema A. et al., 2015, Exp. Astron., 39, 259
Kellermann K. I. et al., 2007, Ap&SS, 311, 231
Kirk J. G., Guthmann A. W., Gallant Y. A., Achterberg A., 2000, ApJ, 542, 235
Komatsu E. et al., 2009, ApJS, 180, 330
Konigl A., 1981, ApJ, 243, 700
Kovalev Y. Y. et al., 2005, AJ, 130, 2473
Kovalev Y. Y., Lobanov A. P., Pushkarev A. B., Zensus J. A., 2008, A&A, 483, 759
Kovalev Y. A. et al., 2014, Cosm. Res., 52, 393
Kovalev Y. Y. et al., 2016, ApJ, 820, L9
Kovalev Y. Y., Petrov L., Plavin A. V., 2017, A&A, 598, L1
Kraus A. et al., 1999, A&A, 344, 807
Kudryavtseva N. A., Gabuzda D. C., Aller M. F., Aller H. D., 2011, MNRAS, 415, 1631
Kutkin A. M. et al., 2014, MNRAS, 437, 3396
Likhachev S. F., Kostenko V. I., Girin I. A., Andrianov A. S., Rudnitskiy A. G., Zharov V. E., 2017, J. Astron. Instrum., 6, 1750004

Lipunov V. et al., 2010, Adv. Astron., 2010, 349171

Lisakov M. M., Kovalev Y. Y., Savolainen T., Hovatta T., Kutkin A. M., 2017, MNRAS, 468, 4478

Lobanov A. P., 1998, A&A, 330, 79

Lobanov A., 2015, A&A, 574, A84

Marcaide J. M., Shapiro I. I., 1984, ApJ, 276, 56

Marscher A. P., 1980, ApJ, 235, 386

Marscher A. P., 2006, in Hughes P. A., Bregman J. N., eds, AIP Conf. Ser. Vol. 856, Relativistic Jets: The Common Physics of AGN, Microquasars, and Gamma-Ray Bursts. Am. Inst. Phys., New York, p. 1, doi:10.1063/1.2356381

Marscher A. P., 2008, in Rector T. A., De Young D. S., eds, ASP Conf. Ser. Vol. 386, Extragalactic Jets: Theory and Observation from Radio to Gamma Ray. Astron. Soc. Pac., San Francisco, p. 437

Max-Moerbeck W., Richards J. L., Hovatta T., Pavlidou V., Pearson T. J., Readhead A. C. S., 2014, MNRAS, 445, 437

Mertens F., Lobanov A. P., Walker R. C., Hardee P. E., 2016, A&A, 595, A54

Napier P. J., 1994, in Robertson J. G., Tango W. J., eds, IAU Symp. Vol. 158, Very High Angular Resolution Imaging. Kluwer, Dordrecht, p. 117

Nilsson K., Charles P. A., Pursimo T., Takalo L. O., Sillanpaeae A., Teerikorpi P., 1996, A&A, 314, 754

Peterson B. M., Wanders I., Horne K., Collier S., Alexander T., Kaspi S., Maoz D., 1998, PASP, 110, 660

Petrov L., Kovalev Y. Y., 2017a, MNRAS, 467, L71

Petrov L., Kovalev Y. Y., 2017b, MNRAS, 471, 3775

Petrov L., Kovalev Y. Y., Fomalont E. B., Gordon D., 2011, AJ, 142, 35

Pushkarev A. B., Kovalev Y. Y., 2015, MNRAS, 452, 4274

Pushkarev A. B., Hovatta T., Kovalev Y. Y., Lister M. L., Lobanov A. P., Savolainen T., Zensus J. A., 2012, A&A, 545, A113

Pushkarev A. B., Kovalev Y. Y., Lister M. L., Savolainen T., 2017, MNRAS, 468, 4992

Pyatunina T. B., Kudryavtseva N. A., Gabuzda D. C., Jorstad S. G., Aller M. F., Aller H. D., Teräsranta H., 2007, MNRAS, 381, 797

Rasmussen C. E., Williams C. K. I., 2005, Gaussian Processes for Machine Learning. The MIT Press

Readhead A. C. S., 1994, ApJ, 426, 51

Richards J. L. et al., 2011, ApJS, 194, 29

Rickett B. J., Lazio T. J. W., Ghigo F. D., 2006, ApJS, 165, 439

Shepherd M. C., 1997, in Hunt G., Payne H., eds, ASP Conf. Ser. Vol. 125, Astronomical Data Analysis Software and Systems VI. Astron. Soc. Pac., San Francisco, p. 77

Sokolovsky K., 2011, PhD thesis, Max-Planck-Institut für Radioastronomie

Sokolovsky K. V. et al., 2010a, preprint (arXiv:1006.3084)

Sokolovsky K. V., Kovalev Y. Y., Lobanov A. P., Savolainen T., Pushkarev A. B., Kadler M., 2010b, preprint (arXiv:1001.2591)

Sokolovsky K. V., Kovalev Y. Y., Pushkarev A. B., Lobanov A. P., 2011, A&A, 532, A38

Spinrad H., Smith H. E., 1975, ApJ, 201, 275

Stickel M., Fried J. W., Kuehr H., 1988, A&A, 198, L13

Valtaoja E., Lähteenmäki A., Teräsranta H., Lainela M., 1999, ApJS, 120, 95

Véron-Cetty M.-P., Véron P., 2010, A&A, 518, A10

Walker R. C., 1995, in Zensus J. A., Diamond P. J., Napier P. J., eds, ASP Conf. Ser. Vol. 82, Very Long Baseline Interferometry and the VLBA. Astron. Soc. Pac., San Francisco, p. 247

Webb J. R., Howard E., Benítez E., Balonek T., McGrath E., Shrader C., Robson I., Jenkins P., 2000, AJ, 120, 41

White R. J., Peterson B. M., 1994, PASP, 106, 879

Yang J., Gurvits L. I., Frey S., Lobanov A. P., 2009, in Zhang S. N., Li Y., Yu Q. J., eds, Proceedings of 10th Asian-Pacific Regional IAU Meeting. National Observatories of China Press, preprint (arXiv:0811.2926)

Zhao W., Hong X.-Y., An T., Jiang D.-R., Zhao J.-H., Gurvits L. I., Yang J., 2011, A&A, 529, A113

This paper has been typeset from a TEX/LATEX file prepared by the author.